Ferrimagnetic structure in the high-pressure phase of α-Mn

Shingo Araki [1,2,*] Kaisei Iwamoto,[2] Kazuto Akiba [1,2] Tatsuo C. Kobayashi [1,2] Koji Munakata [3]
Koji Kaneko [4,5,6] and Toyotaka Osakabe[4]

[1]*Department of Physics, Okayama University, Okayama 700-8530, Japan*

[2]*Graduate School of Natural Science and Technology, Okayama University, Okayama 700-8530, Japan*

[3]*Neutron Science and Technology Center, Comprehensive Research Organization for Science and Society, Tokai, Ibaraki 319-1106, Japan*

[4]*Materials Sciences Research Center, Japan Atomic Energy Agency, Tokai, Ibaraki 319-1195, Japan*

[5]*Advanced Science Research Center, Japan Atomic Energy Agency, Tokai, Ibaraki 319-1195, Japan*

[6]*J-PARC Center, Japan Atomic Energy Agency, Tokai, Ibaraki 319-1195, Japan*

The α-Mn phase exhibits a large anomalous Hall effect (AHE) in its pressure-induced weak ferromagnetic (WFM) state, despite its relatively small spontaneous magnetization of $\sim$0.02 μ_B/Mn. To understand the underlying mechanism behind this AHE, we performed single crystal neutron diffraction measurements at 2.0 GPa to determine the magnetic structure of the WFM phase. Our investigation reveals a ferrimagnetic structure characterized by nearly collinear magnetic moments aligned along the [001] direction at sites I, II, III-1, and IV-1. In contrast, the small moments at sites III-2 and IV-2 lie within the (001) plane. The calculated net magnetization of this magnetic structure, (-0.08 ± 0.10) μ_B/Mn atom, is in agreement with the experimentally determined spontaneous magnetization. The observation of a magnetic reflection at $\boldsymbol{q} = (0, 0, 0)$ satisfies a key condition for the emergence of the AHE.

I. INTRODUCTION

α-Mn exhibits antiferromagnetic (AFM) order below the Néel temperature $T_N = 95$ K. Applying pressure rapidly suppresses T_N, leading to a high-pressure phase above 1.4 GPa with the transition temperature $T_A \sim 50$ K [1–4]. Within this high-pressure phase, we recently discovered a large anomalous Hall effect (AHE) and a weak ferromagnetic (WFM) character [3,4]. Despite a significantly reduced spontaneous magnetization ($\sim$0.02 μ_B/Mn) compared to individual Mn moments in the AFM phase, the anomalous Hall resistivity ρ_{yx}^A reaches approximately half that of elemental Fe, a well-known ferromagnet. Similar large AHEs have been observed in noncollinear antiferromagnetic systems such as Mn_3Sn and Mn_3Ge, where Berry curvature effects are the driving force [5,6]. Since the AFM phase of α-Mn exhibits no AHE, a nonzero contribution from the Berry curvature is anticipated in the WFM phase. The Berry curvature arises due to broken symmetry, similar to ferromagnetic ordering with a magnetic propagation vector $\boldsymbol{q} = (0, 0, 0)$ [7].

α-Mn crystallizes in the cubic space group $I\bar{4}3m$ (No. 217, T_d^3) with four distinct Mn sites (I, II, III, and IV) occupying Wyckoff positions 2a, 8c, 24g, and 24g, respectively. The unit cell contains 58 Mn atoms in total. Despite its complexity, the α-Mn structure exhibits remarkable stability, remaining intact even under extreme pressures of up to 200 GPa [8].

Neutron diffraction reveals magnetic reflections at $\boldsymbol{q} = (0, 0, 1)$ within the AFM phase [9–14], consistent with a non-collinear magnetic structure where each Mn site possesses a distinct magnetic moment [13,14]. This structure, determined by neutron diffraction, exhibits a splitting of sites III and IV into two crystallographically inequivalent subsites. This splitting breaks the threefold rotational symmetry along the $\langle 111 \rangle$ direction, while sites I and II remain unsplit. The size of magnetic moments have the ordering $m_I > m_{II} > m_{III} > m_{IV}$, where m_i denotes the magnitude at site i. The largest moment, m_I, aligns with the [001] direction, with reported values ranging from 1.9 μ_B to 2.8 μ_B [13,14]. The second-largest moment, m_{II}, orients antiparallel to m_I with a slight tilt from the [001] direction. While previous neutron diffraction studies yielded distribution in tilt angles for m_{II} [13,14], a recent NMR study determined it to be $\sim$6° [15]. Furthermore, the splitting of NMR spectra for site II suggests a lowering of symmetry for this site as well in the AFM ordered state [13,14].

Concerning the high-pressure WFM phase, zero-field NMR measurements have been employed to investigate the magnetic structure [16,17]. The NMR frequencies of sites I and II were decreased in the WFM phase compared to the AFM phase, indicating a reduction in the magnitude of the magnetic moments at these sites. For sites III and IV, only the high-frequency tail of the resonance signal was observed, with the peak well below the minimum measurement frequency of $\sim$5 MHz. This suggests that the magnetic

*Contact author: araki@science.okayama-u.ac.jp

moments at sites III and IV in the WFM phase are negligibly small.

To elucidate the magnetic structure of the WFM phase in α-Mn, we conducted neutron diffraction experiments under pressure. Subsequently, the magnetization curve of the WFM phase was measured.

II. EXPERIMENTAL

A large single crystal of α-Mn was grown by Pb flux in a horizontal configuration [18]. The resulting single crystal has dimensions of approximately 1–2 mm^3, representing a significant increase in size compared to our previous single crystal grown by the conventional vertical flux growth method ($\sim$0.1 mm^3) [3,4].

Neutron diffraction measurements on a single crystal were performed on the SENJU time-of-flight Laue diffractometer at BL18, MLF, J-PARC [19]. A hybrid-anvil-type pressure cell was used to apply pressures up to 2.0 GPa [20]. The single-crystal sample, polished to a size of $1.0 \times 1.0 \times 0.4$ mm^3, was placed in an aluminum alloy gasket with the $(01\bar{1})$ plane mounted on the culet surface of the anvil. Glycerin served as the pressure-transmitting medium [21]. The pressure was determined at room temperature using the ruby fluorescence method. Magnetic and nuclear diffraction data were collected at six crystal orientations near the (hkk) reciprocal lattice plane. Data collection was performed at the lowest temperatures of 2.8 K in the WFM phase and 60 K in the paramagnetic phase. Two wavelength bands (second frame, $\lambda = 4.4 \sim 8.8$ Å; 1.5 frame, $\lambda = 2.2 \sim 6.6$ Å) were used to maximize the collection of magnetic Bragg intensities. The exposure times for the second and 1.5 frames were 4 and 6 h, respectively. Temperature evolution was also measured from 2.8–60 K with a shorter acquisition time. Data reduction and correction were performed using the software STARGazer [19].

Magnetization measurements under 2.1 GPa were conducted using an indenter-type high-pressure cell with a ceramic anvil and NiCrAl hole piece [22]. Approximately 1.4 mg of randomly oriented α-Mn single crystals were loaded into the cell along with Daphne oil 7474 [23] as the pressure medium. Magnetization was measured using a superconducting quantum interference device (SQUID) magnetometer (MPMS, Quantum Design). The applied pressure was estimated based on the loading force, using a calibration derived from the superconducting transition temperature of Pb. Magnetization measurements at ambient pressure were conducted with the applied magnetic field aligned along the [001] direction using a SQUID-VSM (Quantum Design).

III. RESULTS AND DISCUSSION

As a first step, the crystal structure at 2.0 GPa was analyzed using nuclear intensity data collected at 60 K ($> T_A$). All observed peaks were successfully indexed to the reported body-centered cubic (BCC) structure, without any sign of secondary phase. The lattice constant was determined to be $a = 8.8284$ Å. The nuclear Bragg peak intensity, $I_{obs}(hkl)$, is described by the following equation:

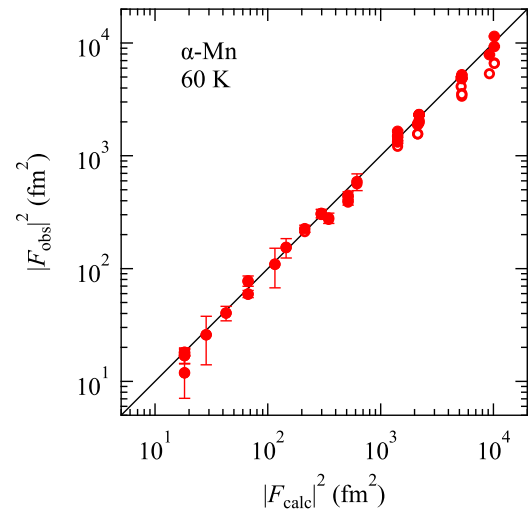$$I_{obs}(hkl) = S\,A(\lambda, hkl)\,E(\lambda, hkl, |F_{obs}|^2)\,L(\theta)\,|F_{obs}|^2, \quad (1)$$

FIG. 1. Relationship between the observed structure factor $|F_{obs}|^2$, calculated from Eq. (1) at 60 K, with and without considering the extinction effect. Filled circles represent $|F_{obs}|^2$ with the extinction correction, while open circles represent $|F_{obs}|^2$ without extinction correction.

where S is the scale factor, $A(\lambda, hkl)$ is the absorption coefficient, $E(\lambda, hkl, |F_{obs}|^2)$ is the extinction parameter, $L(\theta)$ is the Lorentz factor, θ is the scattering angle, and F_{obs} is the observed structure factor. The nuclear structure factor, F_{calc}, calculated from the crystal structure, is given by:

$$F_{calc} = \sum_j b_j\,e^{i\boldsymbol{Q}\cdot\boldsymbol{r}_j}, \quad (2)$$

where the summation is over the unit cell and $b_j = -3.73$ fm is the Mn scattering length. Figure 1 shows a plot of the square of observed and calculated structure factors ($|F_{obs}|^2$ and $|F_{calc}|^2$) at 60 K, with and without extinction correction. The observed structure factors are well explained by the reported BCC structure. Introducing extinction correction further improves the fit for high $|F_{calc}|^2$ values ($>10^3$ fm^2). This refinement is not necessary for the subsequent magnetic analysis. The obtained structure parameters, summarized in Table II, are consistent with those reported at ambient pressure and 4.4 K [13].

Figures 2(a) and 2(b) show the intensity maps of the (hkk) reciprocal lattice plane at 2.8 and 60 K, respectively. Upon cooling, reflections with $h = 2n$ (for all integer k) exhibit a significant intensity increase compared to 60 K, corresponding to the locations of nuclear Bragg peaks (highlighted by bold circles). These reflections are consistent with those allowed by the BCC crystal structure. Notably, no intensity is observed at $h = 2n + 1$ at 2.8 K, where AFM peaks are present at ambient pressure (highlighted by dotted circles). Additionally, no superlattice reflections are observed as well. These results indicate that the magnetic structure in the WFM phase exhibits the same symmetry as the chemical structure, with a magnetic propagation vector $\boldsymbol{q} = (0, 0, 0)$.

Figures 2(c)–2(e) show the temperature dependence of $|F_{obs}|^2$ at (200), (211), and (222) reflections, respectively. The bold horizontal line represents $|F_{calc}|^2$, which is equal to $|F_{obs}|^2$
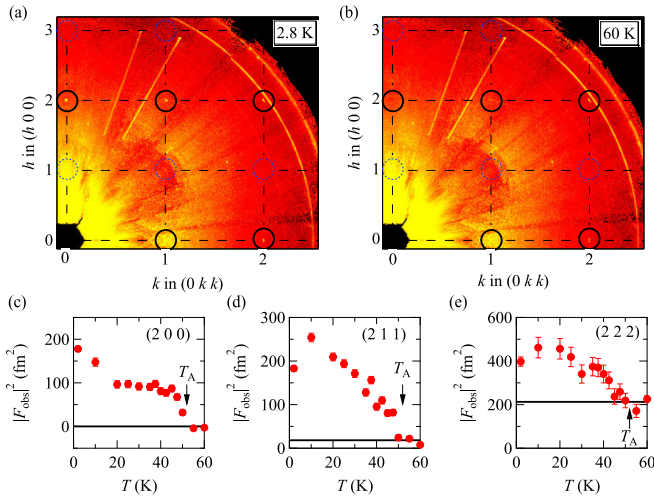
FIG. 2. (a) and (b) Neutron scattering intensity map of the reciprocal (hkk) plane at 2.8 K ($T < T_A$) and 60 K ($T > T_A$), respectively. (c), (d), and (e) Temperature dependence of $|F_{obs}|^2$ at (2 0 0), (2 1 1), and (2 2 2) reflections, respectively.

above T_A. Below T_A, $|F_{obs}|^2$ increases significantly for all three reflections. However, the temperature variations differ, particularly below 20 K, suggesting that the magnetic moments at sites I, II, III, and IV may have distinct temperature dependencies.

Figure 3 shows the calculated and observed magnetic Bragg peak intensities at 2.8 K, represented by $|F_{mag}|^2 = |F_{obs}(2.8K)|^2 - |F_{obs}(60K)|^2$, as magnetic peaks overlap with nuclear ones. Although 23 reflections were observed, their standard deviations are heavily influenced by the underlying nuclear Bragg peaks, which are usually much stronger than magnetic ones. To overcome these difficulties, we employed complementary approaches to obtain reliable results, symmetry analysis, magnetization measurements, and comparison with NMR.

Figure 4 illustrates the possible magnetic space groups derived from the parent $I\bar{4}3m$ structure, assuming nonzero magnetic moments on each Mn site [24–27]. Among the subgroups, the three highest-symmetry magnetic space groups are rhombohedral $R3m'$, orthorhombic $Fm'm2'$, and tetragonal $I\bar{4}2'm'$. The number of fitting parameters, X, for
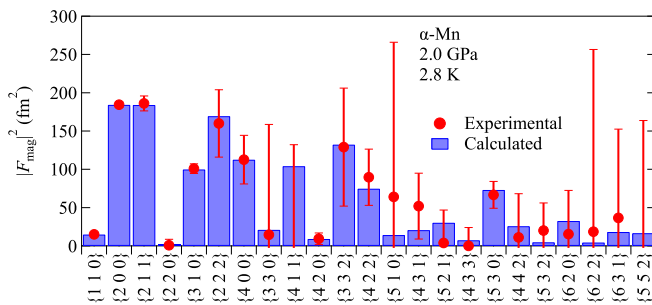

FIG. 3. Bragg peak intensity of magnetic reflections ($|F_{mag}(hkl)|^2$) at 2.8 K. Error bars represent the standard deviation (σ) of magnetic Bragg peak intensity. Blue bars represent the calculated $|F_{mag}|^2$ for the magnetic space group $I\bar{4}2'm'$.
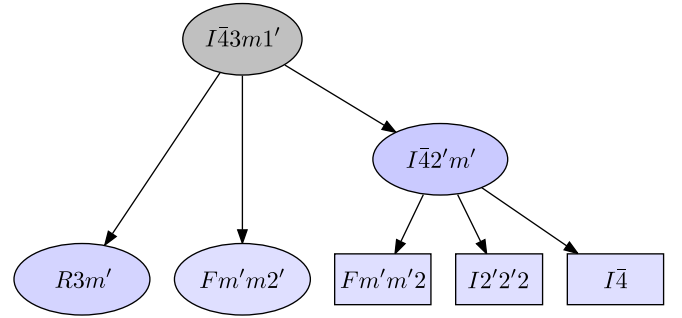

FIG. 4. Possible symmetries for a magnetic structure with a parent structure belonging to space group $I\bar{4}3m$ and a propagation vector $\boldsymbol{q} = (0, 0, 0)$, along with nonzero magnetic moments at each Mn atom site [24–27].

each model is 18, 22, and 13, respectively. Since the magnetic space group exhibits lower symmetry compared to the chemical one, the formation of multiple (e.g., three in the tetragonal case) magnetic domains is expected below the transition temperature (T_A). However, no experimental evidence of anisotropic reflection intensities was observed. This suggests the formation of magnetic domains with equal volume fractions, which is assumed for the following analysis. To identify the most plausible magnetic structure, we employed a least-squares method that minimizes the R factor as follows:

$$R_{res} = \sum_{hkl} \left(\frac{|F_{mag}(hkl)|^2 - |F_{cal}(hkl)|^2}{\sigma(hkl)} \right)^2, \qquad (3)$$

where $|F_{cal}(hkl)|^2$ is the calculated magnetic intensity of the magnetic Bragg peak, given by:

$$|F_{cal}(hkl)|^2 \propto f^2(\boldsymbol{Q}) |M_\perp(\boldsymbol{Q})|^2, \qquad (4)$$

where $f(\boldsymbol{Q})$ is the magnetic form factor of Mn^{2+} and $M_\perp(\boldsymbol{Q})$ is the perpendicular component of the Fourier transform of magnetic moments. The resulting R factors (R_{res} and the weighted R factor, R_w) are summarized in Table I. The $I\bar{4}2'm'$ magnetic space group exhibits the lowest R_{res} (R_w) with the minimum number of fitting parameters, suggesting it as the most likely candidate for the WFM phase in α-Mn among the three highest-symmetry magnetic space groups considered.

Table II summarizes the extracted magnetic moments for the WFM phase in α-Mn. Five of the 13 fitting parameters were found to be statistically indistinguishable from zero within their respective error bars. Neglecting these

TABLE I. Typical reliability factors, magnitude of the magnetic moments at sites I and II, and the net magnetization per Mn atom.

	$R3m'$	$Fm'm2'$	$I\bar{4}2'm'$
R_{res}	8.0	19.2	2.3
R_w (%)	2.2	3.1	1.4
m_I (μ_B)	1.6	0.9	1.84
m_{II-1} (μ_B)	1.1	2.0	0.83
m_{II-2} (μ_B)	1.0	0.6	
$\sum m_z$ (μ_B/Mn)	0.23	0.38	-0.08 ± 0.10

TABLE II. Atomic coordinates determined at 60 K and magnetic moments (μ_B) on each Mn site at 2.8 K.

Site	Wyckoff Position	x	y	z	m_x	m_y	m_z	$|m|$
I	2a	0	0	0	0	0	+1.84(15)	1.84(15)
II	8i	0.318(3)	0.318(3)	0.318(3)	−0.02 (10)	−0.02(10)	−0.83(14)	0.83(14)
III-1	8i	0.358(3)	0.358(3)	0.037(3)	−0.08(9)	−0.08(9)	+0.14(11)	0.20(10)
III-2	16j	0.358(3)	0.037(3)	0.358(3)	−0.27(7)	−0.23(13)	+0.07(13)	0.39(9)
IV-1	8i	0.088(2)	0.088(2)	0.280(6)	−0.04(11)	−0.04(11)	−0.42(11)	0.44(13)
IV-2	16j	0.088(2)	0.280(6)	0.088(2)	−0.19(8)	−0.15(8)	−0.06(10)	0.28(6)

negligible values, the magnetic moments at sites I, II, III-1, and IV-1 exhibit collinear alignment along the [001] direction. Conversely, the moments at sites III-2 and IV-2 lie within the (001) plane. For example, the magnetic moments of site II are expressed as (m_x, m_x, m_z), $(−m_x, m_x, m_z)$, $(m_x, −m_x, m_z)$, and $(−m_x, −m_x, −m_z)$. Consequently, the in-plane (xy) components of the magnetic moments at this site cancel each other, resulting in zero net moment within the plane. However, a finite net moment remains along the z direction. This scenario applies to the other sites as well, resulting in a net magnetic moment with a finite z component only.

Figure 5(a) shows the crystal structure of α-Mn viewed along the [100] direction. Sites I and III-1 (II and IV-1) form layers with z coordinates between −0.038 and 0.038 (0.182 and 0.318), respectively. These layers are highlighted in blue (green) backgrounds. Sites III-2 and IV-2 form a layer with z coordinates between 0.088 and 0.142, highlighted in yellow. Figures 5(c)–5(f) show the magnetic structure of each layer perpendicular to the [001] direction.

Figure 5(f) presents the magnetic structure of the layer containing site I (largest moment) and III-1. Their moments align along [001], resulting in a total magnetic moment of $M_z = (2.4 \pm 0.6)\,\mu_B/5\text{Mn}$ in this layer. Figure 5(d) depicts the layer containing site II (second largest moment) and IV-1. Their moments are aligned along [001], antiparallel to those of sites I and III-1, with a total of $(−5.0 \pm 1.0)\,\mu_B/8\text{Mn}$. Figures 5(c) and 5(e) show the layer containing sites III-2 and IV-2. Their moments are perpendicular to the [001], resulting in a near-zero total magnetic moment.

Figure 5(b) shows the M_z of each layer as a function of its z coordinate along the [001] direction. Note that the number of Mn atoms varies across the different layers. M_z alternates in sign along [001]. The solid curve represents the best fit of a sine function to this variation. The dotted line indicates the non-zero net magnetization along [001]. This finite net magnetization with error is calculated by summing up the m_z of each site listed in Table II, as $(−0.08 \pm 0.10)\,\mu_B/\text{Mn}$. This nonzero net magnetization confirms the presence of spontaneous magnetization within this magnetic structure. Therefore, based on the results of this neutron scattering experiment, the magnetic structure of the WFM phase in α-Mn can be classified as ferrimagnetic.

Figure 6(a) shows the magnetization curve measured at 2.1 GPa. Due to the random orientation of the single-crystal grains, the applied magnetic field effectively averages over all crystallographic directions. The dashed line represents the contribution of the NiCrAl pressure cell component [29]. This line closely resembles the magnetization curve measured at 60 K (above T_A), indicating negligible small magne-

tization of α-Mn at this temperature, consistent with the magnetization observed at ambient pressure [triangle in Figs. 6(a) and 6(c)]. Figure 6(b) highlights the emergence of spontaneous magnetization below $T_A = 52$ K. The magnitude of magnetization gradually increases with decreasing temperature, reaching $M_s = 0.016\,\mu_B/\text{Mn}$ at 4.2 K. This value is in good agreement (within experimental error) with the net magnetization estimated from neutron diffraction for the $I\bar{4}2'm'$ space group, where the magnetic moments are aligned along the [001] direction. Conversely, the net magnetization predicted for the $R3m'$ and the $Fm'm2'$ space groups, as presented in Table I, are incompatible with the observed spontaneous magnetization.

The validity of the proposed $I\bar{4}2'm'$ magnetic structure model was further evaluated through comparison with NMR spectroscopy. Figure 7 presents a plot of the resonance frequency (f) of the NMR signal reported in Ref. [16] against the magnetic moment (m) of each site in the WFM phase at 2.0 GPa, obtained from neutron diffraction. Notably, no NMR signals were detected for sites III and IV in the WFM phase [17]. For comparison, data for the AFM phase at ambient pressure (f reported in Ref. [15], m reported in Refs. [13] and [14]) are also included. Compared to the AFM phase, both m and f for sites I and II in the WFM phase exhibit smaller values. The near-identical f/m ratios for sites I and II in the WFM phase suggest a constant hyperfine coupling constant. Note that the magnetic moments determined for the $R3m'$ and $Fm'm2'$ space groups, as shown in Table I, are inconsistent with the f values obtained from the NMR study.

Despite some data dispersion in the AFM phase, the f/m values exhibit a remarkable similarity between the AMF and WFM phases. This suggests that the hyperfine coupling constants for sites I and II are nearly identical and independent of pressure. Note that the observed decrease in f for sites I and II with increasing pressure [16] directly reflects a pressure-induced decrease in their magnetic moments. While neutron diffraction measurements revealed nonzero magnetic moments at sites III and IV in the WFM phase, no corresponding NMR signals were observed. This suggests that the hyperfine coupling constant for sites III and IV is significantly smaller than that for sites I and II. A possible explanation for this difference lies in the hyperfine field from neighboring Mn sites, as proposed in an NMR study of the AFM phase [15].

α-Mn exhibits pressure-induced weak ferromagnetism (WFM) and antiferromagnetism (AFM) at ambient pressure. Neutron diffraction measurements revealed that the magnetic space groups for the WFM and AFM phases are $I\bar{4}2'm'$ and $I_P\bar{4}2'm'$ [13,14,30], respectively. Notably, both phases share the same crystallographic point group $\bar{4}2m$, which supports

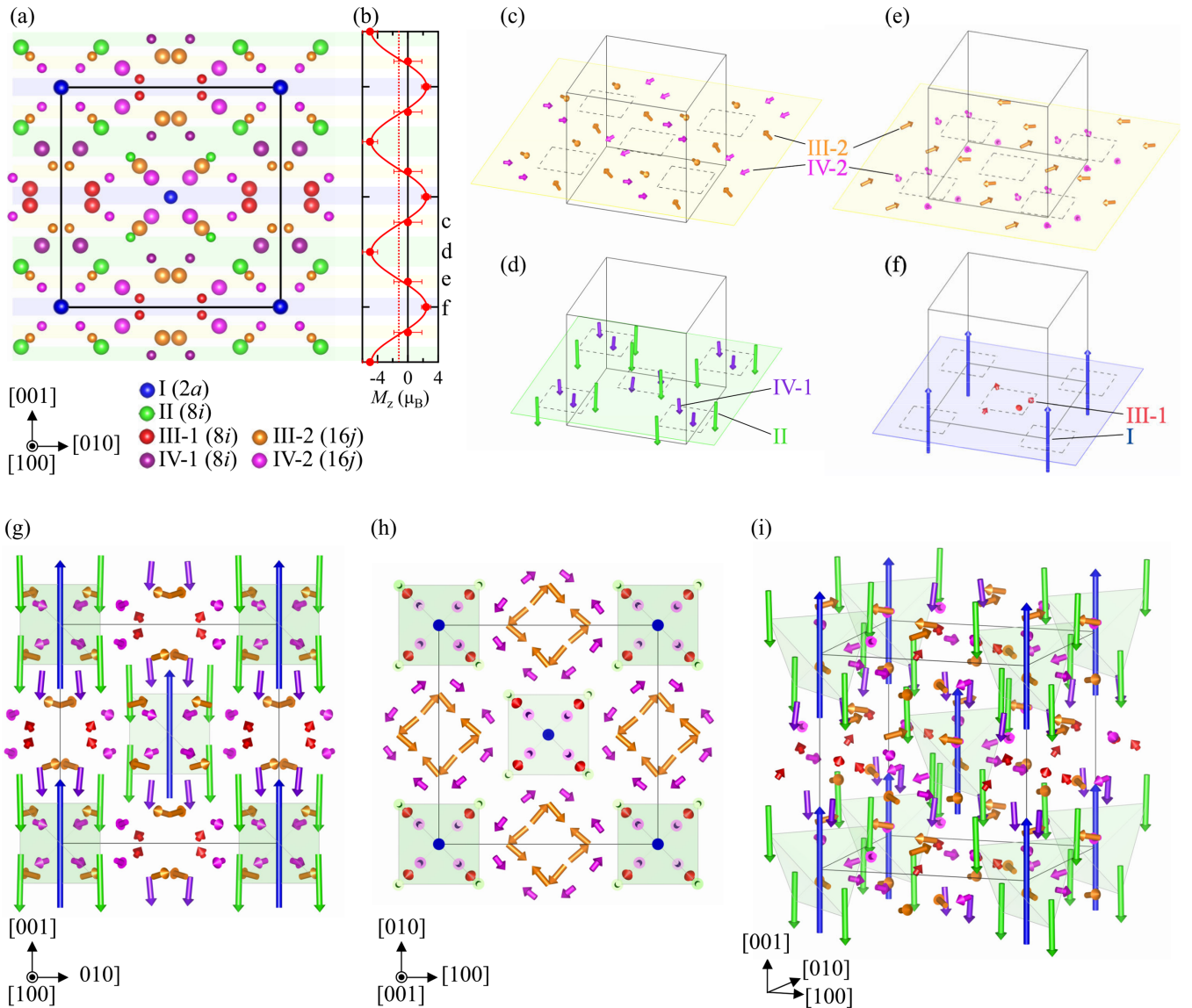FIG. 5. (a) α-Mn crystal structure viewed along the [100] direction, with a unit cell outlined by a square. Different colors represent atoms occupying distinct sites within the $I\bar{4}2'm'$ magnetic space group. Large (small) spheres represent atoms with x coordinates of $-0.25 < x < 0.25$ ($0.25 < x < 0.75$). (b) Total magnetic moment component along the [001] direction (M_z) within the layer perpendicular to [001] in the unit cell (indicated by the colored background). (c)–(e) Magnetic structure within each layer, perpendicular to [001], as indicated on the right side of the (b). Almost collinear magnetic moments (sites I, II, III-1, and IV-1) reside within a broken square surrounding $(0\,0\,z)$ and $(0.5\,0.5\,z)$. Sites III-2 and IV-2 are located outside of the square. (g)–(i) Magnetic structure viewed along the [100] and [001] directions, and a three-dimensional (3D) view, respectively. These crystal structure illustrations were generated using VESTA [28].

the plausibility of the determined magnetic structure of the WFM phase in this study. The magnetic propagation vectors are $q = (0, 0, 0)$ for WFM and $q = (0, 0, 1)$ for AFM. Consequently, only the WFM phase fulfills the necessary conditions for a finite AHE [7]. Large AHEs have been recently reported in materials with weak ferromagnetism, such as NbMnP [31,32], CoNb$_3$S$_6$ [33], Mn$_3$Sn [5], and Mn$_3$Ge [6]. These materials exhibit a small ferromagnetic component (on the order of $10^{-3} \mu_B$) arising from underlying Dzyaloshinskii-Moriya (DM) interactions within their noncollinear magnetic structures. The emergence of a large AHE is highly dependent on the magnetic structure's symmetry. The present result provides valuable constraints on the possible origins of the

large AHE observed in high-pressure α-Mn. Furthermore, this work also opens avenues for theoretical studies on the possible emergence of nonlinear charge transport phenomena in α-Mn under high pressure.

IV. CONCLUSION

Our study reveals a ferrimagnetic structure in the α-Mn WFM phase, characterized by a magnetic propagation vector $q = (0, 0, 0)$ and belonging to the $I\bar{4}2'm'$ magnetic space group. This configuration fulfills a key requirement for a nonzero anomalous Hall response. The magnetic moments at sites I, II, III-1, and IV-1 exhibit collinear alignment
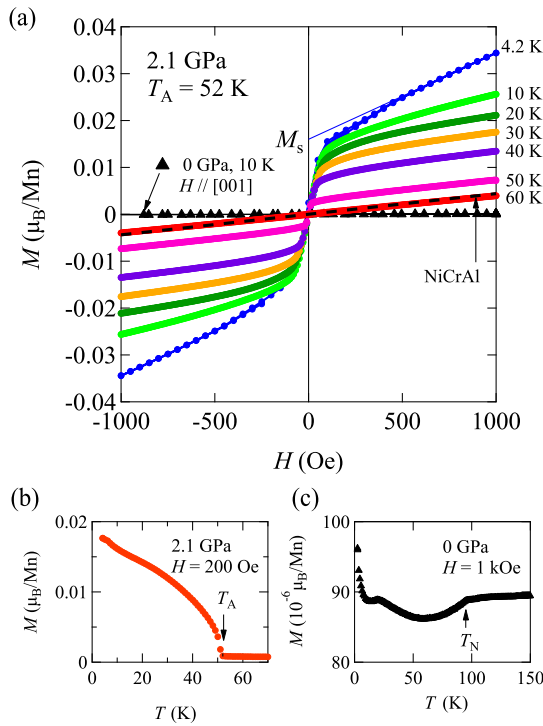
FIG. 6. Magnetization of α-Mn. (a) Isothermal magnetization curves at 2.1 GPa for various temperatures. The curve at 0 GPa is included for comparison. (b), (c) Temperature dependence of magnetization at 2.1 GPa (b) and ambient pressure (c). The applied magnetic fields are 200 Oe and 1 kOe, respectively.
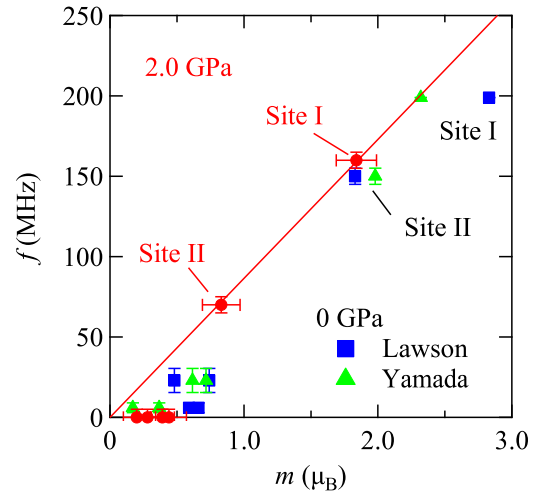

FIG. 7. Relation between the resonance frequency of NMR signal and the magnetic moment determined from the neutron diffraction measurement. The resonance frequency at 2.0 GPa is taken from Ref. [16]. The magnetic moment at 0 GPa is taken from Refs. [14] and [13]. The resonance frequency at 0 GPa is taken from Ref. [15].

along the [001] direction. In contrast, the moments at sites III-2 and IV-2 are perpendicular to this axis. Site I possesses the largest magnetic moment ($1.84 \mu_B$), followed by site II ($0.83 \mu_B$), with these moments being antiparallel. Although relatively small, the magnetic moments at sites III and IV are definitively nonzero, reaching approximately $\sim 0.3 \mu_B$. The net magnetization for the ferrimagnetic structure is $(-0.08 \pm 0.10) \mu_B$/Mn atoms, which is consistent with the observed spontaneous magnetization.

[1] A. Miyake, T. Kanemasa, R. Yagi, T. Kagayama, K. Shimizu, Y. Haga, and Y. Ōnuki, Electrical resistivity measurements of single crystalline α-Mn under high pressure, J. Magn. Magn. Mater. **310**, e222 (2007).

[2] K. Takeda, A. Miyake, K. Shimizu, T. C. Kobayashi, and K. Amaya, Appearance of pressure-induced magnetic phase in α-manganese, J. Phys. Soc. Jpn. **77**, 025001 (2008).

[3] T. Sato, K. Akiba, S. Araki, and T. C. Kobayashi, Pressure-temperature phase diagram of α-Mn, JPS Conf. Proc. **30**, 011030 (2020).

[4] K. Akiba, K. Iwamoto, T. Sato, S. Araki, and T. C. Kobayashi, Anomalous Hall effect triggered by pressure-induced magnetic phase transition in α-Mn, Phys. Rev. Res. **2**, 043090 (2020).

[5] S. Nakatsuji, N. Kiyohara, and T. Higo, Large anomalous Hall effect in a non-collinear antiferromagnet at room temperature, Nature (London) **527**, 212 (2015).

[6] N. Kiyohara, T. Tomita, and S. Nakatsuji, Giant anomalous Hall effect in the chiral antiferromagnet Mn$_3$Ge, Phys. Rev. Appl. **5**, 064009 (2016).

[7] Y. Yanagi, H. Kusunose, T. Nomoto, R. Arita, and M.-T. Suzuki, Generation of modulated magnetic structures based on cluster multipole expansion: Application to α-Mn and CoM$_3$S$_6$, Phys. Rev. B **107**, 014407 (2023).

[8] L. K. Magad-Weiss, A. A. Adeleke, E. Greenberg, V. B. Prakapenka, Y. Yao, and E. Stavrou, High-pressure structural study of α-Mn: Experiments and calculations, Phys. Rev. B **103**, 014101 (2021).

[9] C. G. Shull and M. K. Wilkinson, Neutron diffraction studies of various transition elements, Rev. Mod. Phys. **25**, 100 (1953).

[10] J. S. Kasper and B. W. Roberts, Antiferromagnetic structure of α-manganese and a magnetic structure study of β-manganese, Phys. Rev. **101**, 537 (1956).

[11] J. A. Oberteuffer, J. A. Marcus, L. H. Schwartz, and G. P. Felcher, Magnetic structure of a single crystal of alpha manganese, Phys. Lett. A **28**, 267 (1968).

[12] N. Kunitomi, T. Yamada, Y. Nakai, and Y. Fujii, Preparation of α-manganese single crystals and their physical properties, J. Appl. Phys. **40**, 1265 (1969).

[13] T. Yamada, N. Kunitomi, Y. Nakai, D. E. Cox, and G. Shirane, Magnetic structure of α-Mn, J. Phys. Soc. Jpn. **28**, 615 (1970).

[14] A. C. Lawson, A. C. Larson, M. C. Aronson, S. Johnson, Z. Fisk, P. C. Canfield, J. D. Thompson, and R. B. Von Dreele, Magnetic and crystallographic order in α-manganese, J. Appl. Phys. **76**, 7049 (1994).

[15] M. Manago, G. Motoyama, S. Nishigori, K. Fujiwara, K. Kinjo, S. Kitagawa, K. Ishida, K. Akiba, S. Araki, T. C. Kobayashi, and H. Harima, Site split of antiferromagnetic α-Mn revealed by ^{55}Mn nuclear magnetic resonance, J. Phys. Soc. Jpn. **91**, 113701 (2022).

[16] T. Ito, H. Fukazawa, N. Shioda, Y. Kataoka, T. Ohama, and Y. Kohori, Sudden suppression of internal magnetic fields under high pressure in α-Mn, J. Phys. Soc. Jpn. **90**, 085001 (2021).

[17] N. Shioda, H. Fukazawa, T. Ohama, and Y. Kohori, Zero-field NMR for the pressure-induced phase of α-Mn, J. Phys. Soc. Jpn. **91**, 023709 (2022).

[18] J.-Q. Yan, B. C. Sales, M. A. Susner, and M. A. McGuire, Flux growth in a horizontal configuration: An analog to vapor transport growth, Phys. Rev. Mater. **1**, 023402 (2017).

[19] T. Ohhara, R. Kiyanagi, K. Oikawa, K. Kaneko, T. Kawasaki, I. Tamura, A. Nakao, T. Hanashima, K. Munakata, T. Moyoshi, T. Kuroda, H. Kimura, T. Sakakura, C.-H. Lee, M. Takahashi, K. Ohshima, T. Kiyotani, Y. Noda, and M. Arai, SENJU: A new time-of-flight single-crystal neutron diffractometer at J-PARC, J. Appl. Crystallogr. **49**, 120 (2016).

[20] T. Osakabe, K. Kuwahara, D. Kawana, K. Iwasa, D. Kikuchi, Y. Aoki, M. Kohgi, and H. Sato, Pressure-induced antiferromagnetic order in filled skutterudite PrFe$_4$P$_{12}$ studied by single-crystal high-pressure neutron diffraction, J. Phys. Soc. Jpn. **79**, 034711 (2010).

[21] T. Osakabe and K. Kakurai, Feasibility tests on pressure-transmitting media for single-crystal magnetic neutron diffraction under high pressure, Jpn. J. Appl. Phys. **47**, 6544 (2008).

[22] T. C. Kobayashi, H. Hidaka, H. Kotegawa, K. Fujiwara, and M. I. Eremets, Nonmagnetic indenter-type high-pressure cell for magnetic measurements, Rev. Sci. Instrum. **78**, 023909 (2007).

[23] K. Murata, K. Yokogawa, H. Yoshino, S. Klotz, P. Munsch, A. Irizawa, M. Nishiyama, K. Iizuka, T. Nanba, T. Okada, Y. Shiraga, and S. Aoyama, Pressure transmitting medium Daphne 7474 solidifying at 3.7 GPa at room temperature, Rev. Sci. Instrum. **79**, 085101 (2008).

[24] M. I. Aroyo, J. M. Perez-Mato, D. Orobengoa, E. Tasci, G. de la Flor, and A. Kirov, Crystallography online: Bilbao crystallographic server, Bulg. Chem. Commun. **43**, 183 (2011).

[25] M. I. Aroyo, J. M. Perez-Mato, C. Capillas, E. Kroumova, S. Ivantchev, G. Madariaga, A. Kirov, and H. Wondratschek, Bilbao crystallographic Server: I. Databases and crystallographic computing programs, Z. Kristallogr. Cryst. Mater. **221**, 15 (2006).

[26] M. I. Aroyo, A. Kirov, C. Capillas, J. M. Perez-Mato, and H. Wondratschek, Bilbao crystallographic server. II. representations of crystallographic point groups and space groups, Acta Cryst. A **62**, 115 (2006).

[27] J. M. Perez-Mato, S. V. Gallego, E. S. Tasci, L. Elcoro, G. de la Flor, and M. I. Aroyo, Symmetry-based computational tools for magnetic crystallography, Annu. Rev. Mater. Sci. **45**, 217 (2015).

[28] K. Momma and F. Izumi, VESTA3 for three-dimensional visualization of crystal, volumetric and morphology data, J. Appl. Crystallogr. **44**, 1272 (2011).

[29] Y. Uwatoko, S. Todo, K. Ueda, A. Uchida, M. Kosaka, N. Mori, and T. Matsumoto, Material properties of Ni–Cr–Al alloy and design of a 4 GPa class non-magnetic high-pressure cell, J. Phys.: Condens. Matter **14**, 11291 (2002).

[30] There are two settings or notations currently in use for magnetic space groups. The magnetic space group $I_P\bar{4}2'm'$ in OG setting is also expressed as $P_I\bar{4}2_1c$ in BNS setting.

[31] H. Kotegawa, Y. Kuwata, V. T. N. Huyen, Y. Arai, H. Tou, M. Matsuda, K. Takeda, H. Sugawara, and M.-T. Suzuki, Large anomalous Hall effect and unusual domain switching in an orthorhombic antiferromagnetic material NbMnP, npj Quantum Mater. **8**, 56 (2023).

[32] M. Matsuda, D. Zhang, Y. Kuwata, Q. Zhang, T. Sakurai, H. Ohta, H. Sugawara, K. Takeda, J. Hayashi, and H. Kotegawa, Noncollinear spin structure with weak ferromagnetism in NbMnP, Phys. Rev. B **104**, 174413 (2021).

[33] N. J. Ghimire, A. S. Botana, J. S. Jiang, J. Zhang, Y.-S. Chen, and J. F. Mitchell, Large anomalous Hall effect in the chiral-lattice antiferromagnet CoNb$_3$S$_6$, Nat. Commun. **9**, 3280 (2018).